ГОДИШНИК НА СОФИЙСКИЯ УНИВЕРСИТЕТ „СВ. КЛИМЕНТ ОХРИДСКИ“

ФАКУЛТЕТ ПО МАТЕМАТИКА И ИНФОРМАТИКА
Том 93, 1999

ANNUAIRE DE L'UNIVERSITE DE SOFIA „ST. KLIMENT OHRIDSKI“

FACULTE DE MATHEMATIQUES ET INFORMATIQUE
Tome 93, 1999

NUMERICAL APPROACH TO PATTERN SELECTION IN A MODEL PROBLEM FOR BÉNARD CONVECTION IN FINITE FLUID LAYER

J. PONTES, C. I. CHRISTOV and M. G. VELARDE

Long wave-length pattern formation is studied by means of numerical integration of a fourth-order in space nonlinear evolution equation subjected to Dirichlet lateral boundary conditions. Computationally efficient implicit difference scheme and algorithm are devised employing the method of operator splitting.

The case of Bénard convection in Boussinesq limit is considered. For different sets of the parameters different convective planforms are found: a pattern of hexagons (H^+) with upward flow in their centers, hexagons (H^-) with downward flow in the centers, coexisting hexagons and squares (S), and a case where the squares are selected. In the case when the critical wave-number vanishes (the wave-length diverges) the pattern selected is of a single cell which fills the whole domain under consideration.

Keywords: difference schemes, operator splitting, higher-order diffusion equations, pattern selection, nonlinearity, surface-tension driven convection

MSC 2000: 35K55, 65M06, 74S20, 65Z05

1. INTRODUCTION

Pattern formation in a thin layer of fluid heated from below occurs when the vertical temperature gradient exceeds certain threshold [12, 20, 10, 6]. The nature of the instability and the characteristics of the convective motion depend not only on the fluid parameters but also on the geometric and physical properties of the container. In sufficiently deep cells, or in cells in which the fluid is confined between rigid horizontal boundaries, the convective motion settles when the buoyancy force overcome the viscous forces (Rayleigh-Bénard problem). In sufficiently shallow layers with open surfaces, the inhomogeneities of the surface-tension distribution are responsible for the onset of the motion (Bénard-Marangoni problem) [3, 13]. Depending on whether the horizontal boundaries are good thermal conductors or not, the characteristic wave-length of the convective structure is either comparable to or is much larger than the depth of the cell.

In this work we deal with the problem of pattern selection and the long-term evolution of the planar field in horizontally limited systems, subject to rigid boundary conditions at the sidewalls: $u = \partial u/\partial n = 0$, where u is the temperature.

Different amplitude equations are derived in the literature as simplified models for the convective motion *in lieu* of the full system of the compressible Navier-Stokes (N-S) equations. Here belongs the Swift-Hohenberg (S-H) equation (see, for instance, [6]) and its generalizations [1], as well as the Knobloch equation [8, 9], to mention a few. The main difference between these two models is that the S-H equation has a Lyapunov potential, while the Knobloch equation has not, being thus physically much closer to the original model based on the full Navier-Stokes equations.

Knobloch's equation (1) is very similar to the 2D Navier-Stokes (N-S) system not only as a physical model but as a mathematical structure as well. It is simpler in the sense that it is a scalar equation containing no pressure, and hence no incompressibility constraint has to be satisfied. On the other hand, Eq. (1) is more complicated than the N-S one on the account of the numerous nonlinear terms which make it a multi-parametric model with a rich phenomenology.

Following [5], we employ the method of operator splitting to construct an efficient difference scheme and algorithm for solving the generalized diffusion equation (1) which contains fourth-order spatial derivatives. This is the numerical objective of the present paper. The proximity of the solution to its asymptotic state is assessed via monitoring the L_1-norm of the difference between two consecutive time steps; this norm is sensitive not only to the *changes* in the amplitude of the structure but also to the evolution of its *phase*.

The second objective of the present paper is to obtain physically relevant results. In this instance, the emphasis is placed on three aspects. First, the pattern selection is examined and the results are compared to the existing ones, particularly to those obtained in the framework of the Knobloch's equation. Second, we find numerically the possible non-stationary asymptotic states toward which the system evolves. Third, the long-time evolution of the patterns is tracked. In all these cases the wave-length and the spectral content of the patterns in terms of Fourier modes are thoroughly examined.

2. POSING THE PROBLEM

Chapman & Proctor [4] and Sivashinsky[15, 16] introduced an equation to describe the long wave-length pattern formation induced by buoyancy or by surface-tension instabilities in a thin layer of fluid. This equation was later generalized by Knobloch to the form

$$\frac{\partial u}{\partial t} = \alpha u - \mu \nabla^2 u - \nabla^4 u + \kappa \nabla \cdot |\nabla u|^2 \nabla u \\ + \beta \nabla \cdot \nabla^2 u \nabla u - \gamma \nabla \cdot u \nabla u + \delta \nabla^2 |\nabla u|^2. \tag{1}$$

Here, $u(x, y, t)$ is the horizontal planform of the temperature deviation from the conductive profile, x, y and t are *slow* variables, μ is the scaled bifurcation parameter, and α represents the effect of finite thermal conductivity of the horizontal boundaries, or finite Biot number. When the boundary conditions at the top and bottom of layer are not identical, then $\beta \neq 0$ and $\delta \neq 0$. Respectively, if non-Boussinesq effects are to be taken into account, one has $\gamma \neq 0$. In the present paper we do not deal with non-Boussinesq effects, hence, we set $\gamma = 0$. The coefficient κ can always be set to ± 1, see [8], except for solidification in binary alloys, where it vanishes. Specifically, in the case of Bénard's convection, $\kappa = +1$.

Knobloch considered modes forming square and hexagonal lattices, but he did not address the question of relative stability between squares and hexagons, and suggested that the problem should be studied numerically. He did not consider the case in which $\kappa = -1$, nor did he interrogate the non-stationary patterns that could emerge due to the non-potential character of Eq. (1). Shtilman & Sivashinsky [14] integrated Eq. (1) numerically in a square region of approximately 4×4 wavelengths, subjected to periodic boundary conditions. They set $\gamma = 0$, $\beta > \delta$ and obtained a structure of positive hexagons quite in accordance with experimental findings in Bénard–Marangoni convection and the analytical results of Knobloch for this range of parameters. Recently, Skeldon & Silber [17] extended the stability analysis performed by Knobloch and found some scenarios, where transition from hexagons to rectangles may occur. In some cases, these authors found that near onset some more exotic spatially periodic planforms are preferred to the usual rolls, squares and hexagons.

The existing results, concerning pattern selection in the framework of the dynamics represented by Eq. (1), can be summarized as follows:

- Square lattices:
  - Squares are stable if $\beta = \gamma = \delta = 0$;
  - Rolls are stable if $\beta = \delta \neq 0$ and $\gamma \neq 0$;
  - Rolls are stable for $\beta \neq 0$ and $\beta - \delta \neq 0$ if $\gamma = 0$.
- Hexagonal lattices:
  - Hexagons are stable if $\beta = \gamma = \delta = 0$;
  - If $|\beta + \gamma/q_c^2 - \delta| \ll |\beta|, |\delta|, |\gamma| = \mathcal{O}(1)$, the hexagons are stable at low amplitudes, having upward (H^+) or downward (H^-) flows in their centers depending on the sign of $(\beta + \gamma/q_c^2 - \delta)$, while the rolls are stable at larger amplitudes;
  - H^+ and H^- coexist at large amplitudes if $|\beta|, |\gamma|, |\delta| \ll 1$.

In this study we consider the Bénard convection in Boussinesq approximation when $\kappa = +1$ and $\gamma = 0$. Only in one of the calculations for the squared tessellations we use $\kappa = -1$ for the sake of comparison of the physical mechanisms. The simulations are conducted in the above selected parameter range for a square box with horizontal dimensions 150×150 (approximately 20 to 23 wave-lengths per side). Eq. (1) is integrated numerically in the points of a square grid of 402×402 points, which means roughly 17.5 points per wave-length. This is a significant improvement of the resolution in comparison with the works from the literature. The time-step used in our simulations is $\Delta t = 0.1$.

Section 4.1 presents the results concerning H^+ or H^- hexagons. Section 4.2 discusses squared tessellations S, obtained both with $\kappa = +1$ and $\kappa = -1$. Section 4.3 deals with the problem of the coexistence between squares and hexagons. In Section 4.4 the result of a simulation for $\alpha = 0$ is presented. This is a case when the critical wave-length diverges (zero critical wave-number).

3. NUMERICAL SCHEME

Following [5], we use here the idea of operator splitting to create efficient scheme which will allow extensive numerical experiment. In order to secure the desired properties of the operators to be inverted, we use a semi-implicit approximation of the nonlinear terms. First we recast the original PDE to a form stemming from a first order discrete representation of the time derivative:

$$\frac{u^{n+1} - u^n}{\Delta t} = \left(\Lambda_x^n + \Lambda_y^n\right) u^{n+1} + f^n, \tag{2}$$

or

$$\left[I - \left(\Lambda_x^n + \Lambda_y^n\right)\right] u^{n+1} = \Delta t \left(u^n + f^n\right), \tag{3}$$

where I is the identity operator, and u^n, u^{n+1} stand for the dependent variable on the respective time stage. Respectively, the operators Λ_x^n, Λ_y^n and the function f^n are defined as follows:

$$\Lambda_x^n = \frac{\alpha}{2} - \frac{\partial^4}{\partial x^4} + \kappa \frac{\partial}{\partial x}\left(|\nabla u^n|^2 \frac{\partial}{\partial x}\right),$$

$$\Lambda_y^n = \frac{\alpha}{2} - \frac{\partial^4}{\partial y^4} + \kappa \frac{\partial}{\partial y}\left(|\nabla u^n|^2 \frac{\partial}{\partial y}\right),$$

$$f^n = -2\frac{\partial^4 u^n}{\partial x^2 \partial y^2} - \mu \nabla^2 u^n + \beta \nabla \cdot \nabla^2 u^n \nabla u^n - \gamma \nabla \cdot u^n \nabla u^n + \delta \nabla^2 |\nabla u^n|^2.$$

Here it becomes clear why the scheme is called "semi-implicit". The nonlinear terms involving the third derivatives and proportional to the coefficient k are taken in divergent form in which the coefficients are from the "old" time-stage, while the derivatives itself are treated implicitly. Generally speaking, some more terms can be approximated implicitly, but such an approximation will destroy the negative definiteness of the operators to be inverted at each time step. For this reason we leave them on the "old" time stage.

Now the full inversion of the operator $[I - (\Lambda_x^n + \Lambda_y^n)]$ requires a considerable computational effort. We use here the operator-splitting scheme of *stabilizing correction*. We split Eq. (3) into the following two half-time steps [5]:

$$\begin{aligned} (I - \Delta t\, \Lambda_x^n)\, \tilde{u} &= \left(I + \Delta t\, \Lambda_y^n\right) u^n + \Delta t\, f^n, \qquad (4) \\ \left(I - \Delta t\, \Lambda_y^n\right) u^{n+1} &= \tilde{u} - \Delta t\, \Lambda_y^n\, u^n. \qquad (5) \end{aligned}$$

Upon applying the operator $(I - \Delta t\, \Lambda_x^n)$ to Eq. (5) and adding the result to Eq. (4) one obtains

$$\left(I + (\Delta t)^2 \Lambda_x^n \Lambda_y^n\right) \frac{u^{n+1} - u^n}{\Delta t} = \left(\Lambda_x^n + \Lambda_y^n\right) u^{n+1} + f^n,$$

which means that within the second order approximation in time, the splitting scheme is equivalent to the original semi-explicit scheme (2). The advantage of the splitting is twofold. The operator in the left-hand side of Eqs. (4) and (5) displays a penta-diagonal structure when the space operators are approximated to second order on the difference level. The elements of these operators are just numbers and not matrices, as in the case of Eq. (3). Second, Eq. (4) can be solved line by line and Eq. (5) can be solved column by column, reducing considerably the storage requirements. The five-diagonal systems were then solved by Gaussian elimination with pivoting. The scheme (4), (5) generalizes for the fourth-order diffusion operators the classical operator splitting scheme of *stabilizing correction* [7, 21].

When a stationary pattern is investigated, the boundary conditions and coefficients of equation do not depend explicitly on the time t and the computed transient solution should converge to the steady solution unless a chaotic régime onsets. Of prime importance for computing the steady solutions is the selection of the criterion to judge whether the convergence is reached since the *amplitude* and the *phase dynamics* of the pattern evolve on different time scales. The phase evolves much slower than the amplitude does. Then the uniform norm of the difference between two consecutive iterations will follow the rate with which the maximal amplitude of the transient approaches the maximal amplitude of the steady solution. Using an uniform norm would send a false signal that solution converges long before the phase pattern reaches its stationary shape. Following [5], we track the time evolution of patterns by monitoring an L_1-type of norm which measures the rate of change of the *distance* between two successive states of the system. The L_1-norm is sensitive to the evolution of both the amplitude and the phase:

$$L_1 = \frac{1}{\Delta t} \frac{\sum_{i,j} |u_{i,j}^{n+1} - u_{i,j}^n|}{\sum_{i,j} |u^{n+1}|}, \qquad (6)$$

where the sums are made over all interior points of the grid.

4. NUMERICAL RESULTS

In this section we present the results of our numerical simulations of the Knobloch equation (1). All simulations begin at $t = 0$, from a random initial condition. As already mentioned in the foregoing discussion, we focus our attention on the case $k > 0$. We choose without loosing the generality $k = 1$. Only in one of the runs we use $\kappa = -1$ for the sake of comparison. More exhaustive treatment of the non-Bénard case $\kappa < 0$ is due elsewhere.

We consider only the cases when $\alpha \leq 0$, which means that there is no energy input proportional to the temperature u. For $\alpha < 0$ the said term accounts for a linear attenuation of the solution. Then for the dispersion relation for the Fourier modes of the linear part of Eq. (1) in unbounded region and for the interval of unstable wave-numbers we get

$$s = \alpha + \mu q^2 - q^4 \,, \quad \frac{\mu}{2} - \sqrt{\frac{\mu^2}{4} - |\alpha|} < q < \frac{\mu}{2} + \sqrt{\frac{\mu^2}{4} - |\alpha|} \,,$$

where the negative sign of α is acknowledged.

One sees that there is a whole band of unstable modes. The fastest growing mode (the largest positive s) is $q_m = \sqrt{\mu/2}$ with exponent $s_m = \alpha + \frac{1}{2}\sqrt{\mu^2}$. In most of the cases treated in the present work q_m does not have much impact on the results and cannot effectively serve as a representative critical number. For this reason we propose a somewhat more elaborate definition of the critical wave number q_c. Namely, we find the value of μ for which $s_m = 0$, i.e. the value for which an unstable mode first appears. Clearly, this can happen only for $\mu = 2\sqrt{|\alpha|}$. Then we call "critical wave-number" the magnitude of q_m for this particular value of μ, $q_c = \sqrt{|\alpha|}$. As it will become clear in what follows, this critical wave-number is rather relevant to the wave motions under consideration.

The hexagon pattern with an upward flow in the centers of hexagons is denoted by H^+. Respectively, H^- stands for the pattern in which the flow in the centers of hexagons is downward. The grey shades of the plots are selected between white (regions with the most rapid upward flow) and black (the fastest downward flow). In order to gather more information about the motion, the Fourier transform of the pattern is shown in the figures. To this end, we include also a panel in the figures showing the sum of the amplitudes of all wave-numbers A in the interval between q and $q + \Delta q$, regardless to their orientation. Respectively, Δq is the grid spacing of the discrete Fourier transform. The respective result is depicted in the lowest panels of the figure as a function of (q/q_c). The position q_f of the peak identifies the fundamental mode of the structure which is, in general, different from the critical mode q_c.

4.1. FINITE WAVE-LENGTH HEXAGONS

The starting point of our simulations is the numerical work [14]. We adopt the same values used by those authors for the coefficients of the quadratic terms, namely $\beta = -0.125\sqrt{7}$, $\alpha = -0.8$ and $\mu = 2.7$.

For $\delta = -0.75\sqrt{7} < 0$, the system evolves into a pattern of positive hexagons which we designate as H^+. The structure obtained at the end of the simulation ($t = 19050$) is shown in the top-left panel of Fig. 1.

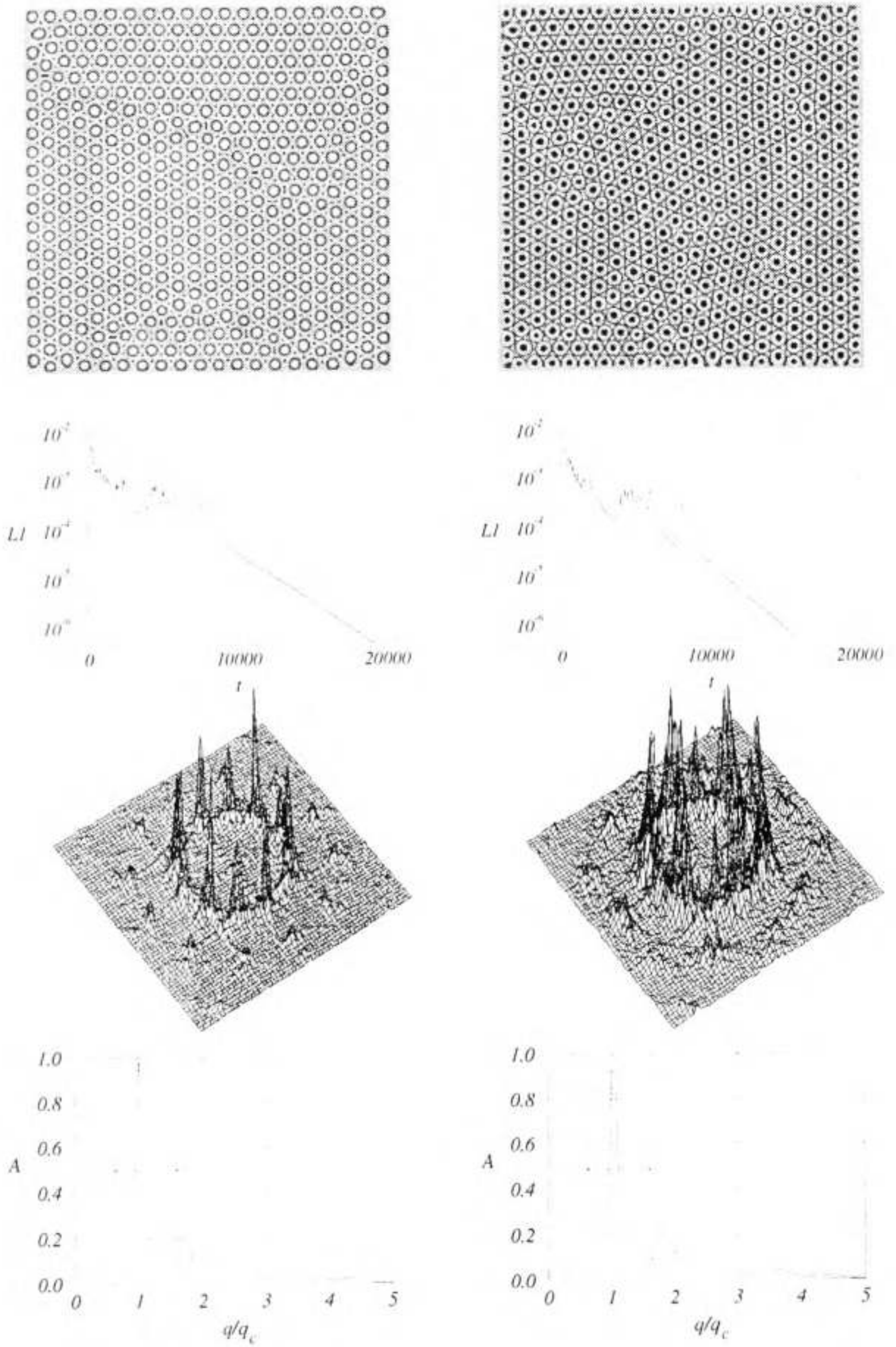

Fig. 1. Hexagons in square geometry for $\mu = 2.7$, $\alpha = -0.8$, $\beta = -0.125\sqrt{7}$. Left panels: H^+ at $t = 19050$ for $\delta = -0.75\sqrt{7}$. Right panels: H^- at $t = 15990$ for $\delta = 0.75\sqrt{7}$. From top to bottom: the pattern; the time evolution of L_1-norm; the Fourier transform; the wave-number content of the pattern

In the beginning, the small scales existing in the random initial condition are rapidly attenuated due to the filtering action of the dissipative part $\alpha - \nabla^4$ of the linear operator of Eq. (1). The most significant growth of the amplitude occurs in this phase and the decrease of the L_1-norm is very fast. The second phase is essential for the pattern evolution. It is characterized by an irregular behaviour of L_1 which on average decays much slower than in the initial stage. As the structure evolves, new cells are created or annihilated, dislocations move, and grains slide relative to each other. The number of defects usually diminishes as longer space correlations are created and the whole pattern moves. Tribelsky *et al.* show in [19] that just before and after a cell is created or annihilated, the evolution accelerates according to a power law. The peaks of the $L_1(t)$-curve reflect the time moments when *qualitative* changes occur in the pattern. Eventually, the system finds a configuration where further qualitative changes become extremely difficult and then the third stage of evolution begins characterized by a sustained exponential decay of the L_1-norm. We terminate the simulation after the L_1-norm decreases another order of magnitude since the moment of onset of the third phase of the evolution.

The pattern shown in the top-left panel of Fig. 1 contains three *grains*, the first one being adjacent to the upper boundary and having one of the axis of the lattice parallel to that wall. A second smaller grain of the same lattice orientation occupies a part of the lower wall. The third (the biggest) grain occupies the central part of the box and presents a lattice rotated by an angle of $\pi/6$ with respect to the other two. Several *hepta-penta* defects can be observed on the grain boundaries.

The third panel in the left column of Fig. 1 shows the core part of Fourier modes of the pattern at the end of the simulation $t = 19050$. Twelve peaks can be observed in the ring of fundamental modes, reflecting the existence of lattices with *two* orientations. In addition, this figure shows also the existence of secondary peaks (the bottom-left panel in Fig. 1) which can be explained using the arguments presented graphically in Fig. 2.

In order to identify the relative importance of the amplitude of the modes, irrespective to their orientation, we computed the sum (denoted by A) of the amplitudes found in circular rings of the Fourier transform centered in $q = 0$ and limited by

$$n\Delta q - \Delta q/2 \leq q < n\Delta q + \Delta q/2,$$

where $\Delta q = 2\pi/l$ and $n = 1, 2, \ldots$ The values of A, obtained as a function of q/q_c and normalized by $\max(A)$, are plotted in the bottom-left panel of Fig. 1. The curve displays an absolute maximum in $q/q_c = 0.98$, which we define as q_f/q_c, with q_f being the *fundamental* wave-number of the pattern. There are also several smaller peaks associated with modes $\sqrt{3}\, q_f$, $2\, q_f$, $\sqrt{7}\, q_f$ and $2\sqrt{3}\, q_f$. It is seen that the fundamental *wave-length* of the pattern is smaller than the critical one. We also outline by dashed vertical lines the limits on the band of linearly unstable modes. It can be seen that there are secondary peaks *out* of that band, i.e. active modes with negative eigenvalue. The next four relevant peaks are located in $q/q_c = \sqrt{3}, q_f/q_c$, $2q_f/q_c$, $2.65 \approx \sqrt{7}, q_f/q_c$ and $2\sqrt{3}\, q_f/q_c$. The amplitude of the peaks diminishes as q/q_c increases due to the fact that the eigenvalue of a mode becomes more and more negative, as the distance to the band of linearly unstable modes increases. This reveals an important signature of weakly-nonlinear systems: the interaction between modes promoted by the nonlinear dynamics merely introduces corrections to the fundamental modes, the latter being the most important in defining the essential features of the structure.

Thess & Bestehorn [18] found by direct integration of Navier-Stokes equations that an H^--structure appears in Bénard-Marangoni convection if the Prandtl number of the fluid is smaller than a critical value. We encounter negative hexagons H^- for positive $\delta = 0.75\sqrt{7}$. The size of the system and the values of the rest of the parameters are the same as in the preceding case H^+, except for the coefficient δ, for which we took the opposite sign.

The pertinent drawings are shown in the right panels of Fig. 1. In this case the end of the simulation appears at $t = 15990$. Now the system develops a more complex structure than in the H^+-case, which is also reflected by the Fourier transform of the pattern. Several *dislocations* and *hepta-penta defects* are observed. Yet, the curve $L_1(t)$ displays the same qualitative features found in the previous case and the time interval required to attain a sustained exponential decay of $L_1(t)$ is also comparable ($t = 15990$ here and $t = 19050$ in the previous configuration). The higher level of disorder of the H^--case is compatible with the higher forcing, applied to the system, which is reflected by a somewhat wider band of linearly unstable modes. The bottom-right panel of Fig. 1 shows that H^- contains the same structure of Fourier modes as the one found for H^+. The fundamental wave-number of the pattern is greater than the critical wave-number, namely $q_f = 1.03\, q_c$.

Fig. 2 focuses on an extended area around the core part of the Fourier transform of the H^+-pattern shown in the respective panels of Fig. 1. Fig. 2 is constructed using a nonlinear scale of gray shades, in order to enhance the weaker peaks for better observation. It is seen that the peaks fall in five concentric circumferences, whose diameters follow the same relations found for the abscissa of the peaks shown in the lowermost panels of Fig. 1. The first one (1) contains the fundamental modes of the pattern, q_f. Six directions (12 peaks) are observed on this circumference, due to the existence of grains with *two* orientations in the pattern under consideration. The second circumference (2) with radius $q = \sqrt{3}\, q_f$ contains wave-vectors generated by the interaction of fundamental modes of the hexagonal lattice (see also Fig. 2(b)). The third circumference (3) contains the second harmonic of the structure $2\, q_f$. The fourth circumference (4) with radius $q = \sqrt{7}\, q_f$ contains modes generated by the interaction of $\mathbf{q}_f$ and $2\,\mathbf{q}_f$, forming an angle of $\pi/3$. Two different orientations are possible in each $\pi/3$ sector leading to the existence of 12 *pairs* of peaks in this circumference, see Fig. 2(b) and Fig. 2(c). The fifth circumference contains modes with wave-number $q = 2\sqrt{3}\, q_f$. Fig. 2(d) displays a scheme of the pattern in the physical space as contained in each cell.

Twelve peaks can be observed in circumferences # 2, 3 and 5, but circumference # 4 contains twelve *pairs* of peaks. Fig. 2(b) and Fig. 2(c) clarify the origin of these peaks.

Fig. 2(b) shows a hexagon in the Fourier space composed of fundamental modes. The interaction of two aligned fundamental modes results in the second

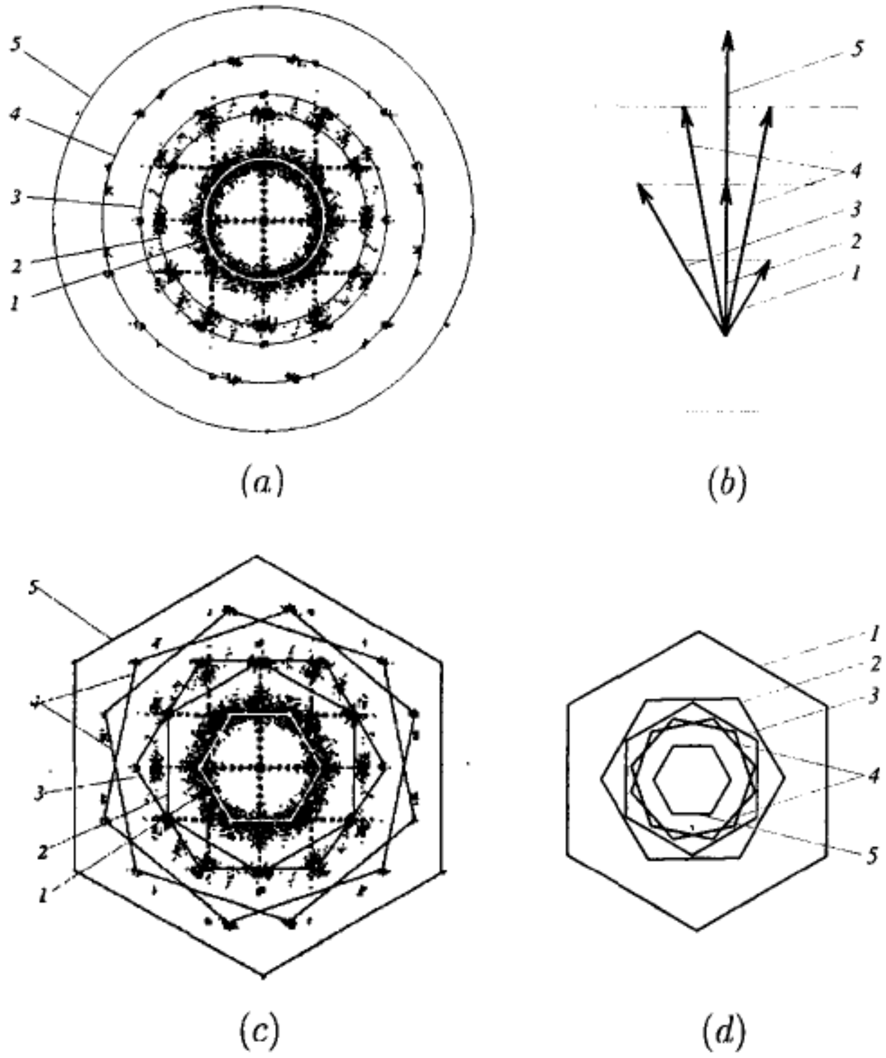

Fig. 2. H^+ in square geometry

harmonic, the interaction of two wave-vectors $\mathbf{q}_f$, forming an angle of $\pi/3$, gives a mode with $q = \sqrt{3}\,q_f$, the interaction of the latter one with itself originates the mode $2\sqrt{3}\,q_f$ and the interaction of a $\sqrt{3}\,q_f$-mode with a fundamental one creates a $\sqrt{7}\,q_f$-mode. In this case there are *two* possibilities in each $\pi/3$ sector. This is why twelve pairs of peaks appear in the circumference # 4.

Fig. 2(c) shows the hexagons in Fourier space, obtained by linking the peaks associated to one of the lattices of the pattern. Fig. 2(d) shows a scheme of a convective cell in the configurational space. Thus we compare the normalized fundamental mode q_f/q_c of the pattern, with the normalized average mode q_a/q_c, where the average mode is defined as

$$q_a = 2\pi\sqrt{\frac{N}{S_a}}\,, \tag{7}$$

where N is the number of cells in the pattern, and S_a is the area of the box.

Due to the existence of empty spaces at the grain boundaries, close to the sidewalls, the above estimate gives as a rule an average wave-number smaller than

q_f. In addition, the pattern contains some cells (like the heptagons) which are larger than the average cell.

4.2. FINITE WAVE-LENGTH SQUARES

We turn now to the question of identifying the conditions leading to square tessellations. Knobloch [9] shows that squares are stable when the system is a Boussinesq fluid with symmetric horizontal boundaries ($\beta = \gamma = \delta = 0$). Shtilman & Sivashinsky [14] obtain the same result by numerically integrating Eq. (1) in a 4×4 wave-length box assuming periodic boundary conditions. The squares can also occur when $\beta = \delta \neq 0$. We consider two configurations of parameters, one of them with $\kappa = +1$ and the other one with $\kappa = -1$.

The case $\kappa = +1$ evolves until $t = 41100$. The high forcing, applied to the system ($\mu - \mu_c = 0.602$), justifies the rather disordered structure obtained in this case (see the left panels in Fig. 3). This behavior is captured also by the Fourier transform. The most conspicuous feature of the pattern is the orientation of the dominant lattice parallel to the diagonals of the box (note that it is parallel to the sidewalls in the case $\kappa = -1$). The normalized fundamental mode is $q_f/q_c = 1$. The consecutive peaks are associated with the modes $\sqrt{2}\,q_f$, $2q_f$, $\sqrt{5}\,q_f$ and $3\,q_f$.

The pattern obtained for $\kappa = -1$ (right column of panels in Fig. 3) displays an almost perfect structure, possibly due to the lower forcing applied to the system. It consists of essentially one *grain* with several defects (*dislocations*). The almost perfect structure of the pattern is reflected by a very clear but rich Fourier spectra. There is no circle of fundamental modes. The inner part of the transform displays a *squared* geometry. Fundamental modes are found only in the directions parallel to the sidewalls and — as observed in the early stages of evolution — a second lattice, parallel to the diagonals of the box, coexists with the dominant lattice. The secondary lattice of modes clearly stems from the interaction of two orthogonal fundamental modes. The bottom-right panel of Fig. 3 shows that the normalized fundamental mode is $q_f/q_c = 1.01$, and several subsequent peaks, located at $\sqrt{2}\,q_f/q_c$, $2q_f/q_c$, $2.23q_f/q_c \approx \sqrt{5}\,q_f/q_c$ and $3q_f/q_c$. It is interesting to mention that the modes with $q = 2\sqrt{2}\,q_f$, which have a wave-vector shorter than $3q_f$, do not survive.

Among the cases, discussed in the present work, this is the most demanding in terms of computational effort, requiring 2×10^6 steps to attain the convergence to the steady solution, $t = 200000$ with time increment $\Delta t = 0.1$.

4.3. COEXISTENCE OF FINITE WAVE-LENGTH SQUARES AND HEXAGONS

The results from the previous sections show that hexagons are selected if β differs significantly from δ and that squares appear when $\beta = \delta$. Then the natural question is whether hexagons and squares can coexist if β differs slightly from δ. The second question is of whether or not H^+ and H^- can coexist if $|\beta|$, $|\delta| \ll 1$.

The answer to the first question is affirmative. The hexagons and squares do coexist when the value of β is in the vicinity of δ. Furthermore, the hexagons are

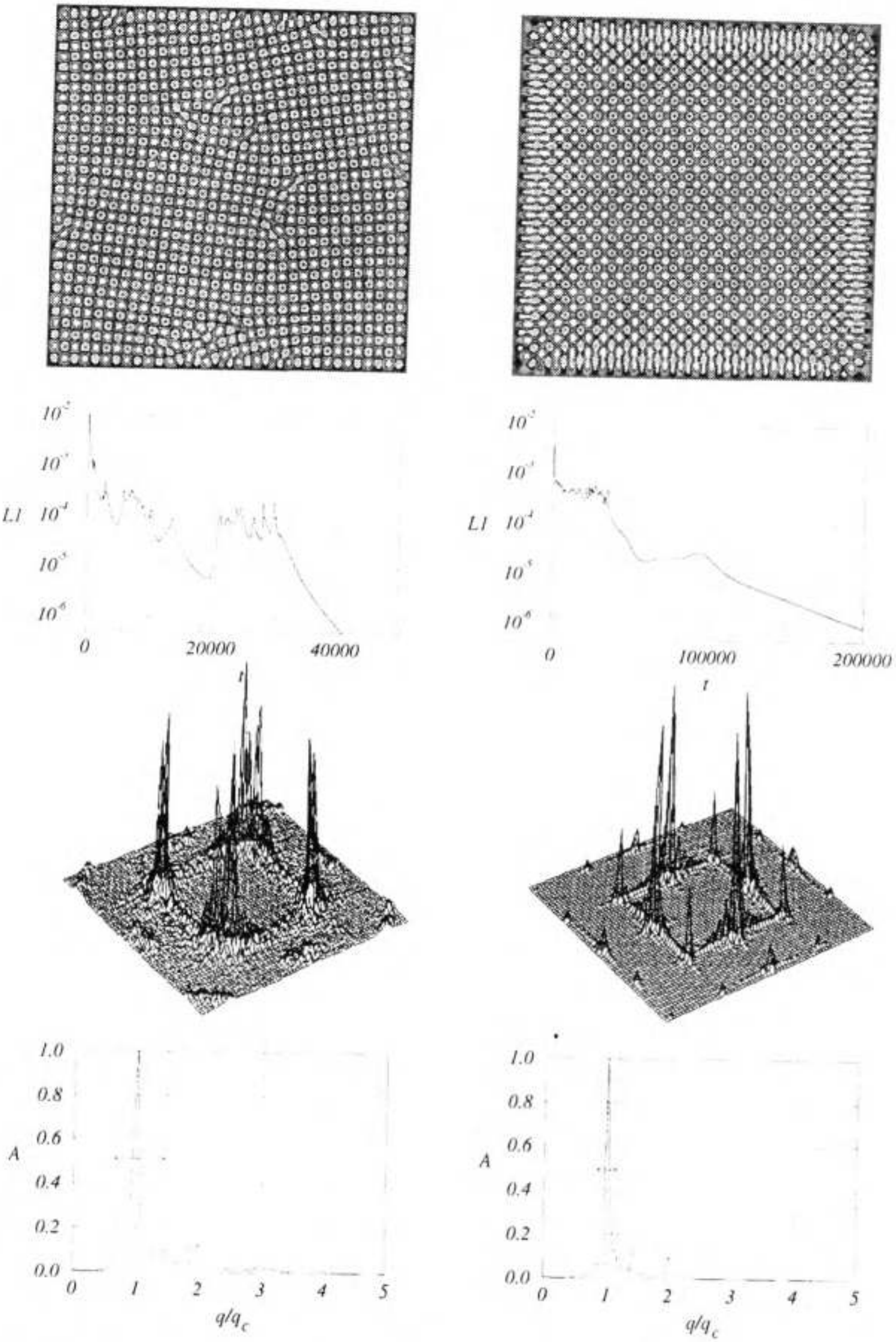

Fig. 3. Squared tessellations. Left panels: S-pattern for $\kappa = +1$ at $t = 41100$ and $\mu = 2.5$, $\alpha = -0.9$, $\beta = \delta = -0.25\sqrt{7}$. Right panel: S-pattern for $\kappa = -1$ at $t = 200000$ for $\mu = 2.0$, $\alpha = -0.9$, $\beta = \delta = -3\sqrt{7}$. From top to bottom: the pattern; the time evolution of L_1-norm; Fourier transform; wave-number content of the pattern shown

positive or negative, depending on the sign of $(\beta - \delta)$, exactly as in the case of the single-pattern tessellations, studied in Section 3.1. However, the conditions for the coexistence of both patterns appear to be much less robust than those that define a single pattern. We find that the coexistence of patterns depends not only on the coefficients of the quadratic terms of Eq. (1) but also on the magnitude of the forcing applied and on the system size, as well. A change in one of these parameters may lead to the collapse of one of the patterns. For instance, with the increase of the forcing, the dominant pattern changes from hexagons to squares. This result was also obtained in [2] by direct integration of the three-dimensional Navier-Stokes equations. In [11] the competition between hexagons and squares in a generalized Swift-Hohenberg equation was studied. It was found there that the front between competing patterns must be perpendicular to their corresponding modes in order to be stable.

The answer to the second question is negative. We do not find a coexistence of positive and negative hexagons. Squares emerge in the neighbourhood of the point where the transition $H^+ \longrightarrow H^-$ occurs, i.e. in the point where the sign of $(\beta - \delta)$ changes, and the transition occurs in the form $H^+ \longrightarrow S \longrightarrow H^-$, or *vice versa*. Besides, one of the hexagon types disappears *before* the onset of the other, and the squares are the only stable pattern in the case when $\beta = \delta$.

As in all of the previous figures the top panels of Fig. 4 show the state of the system at the end of the simulation. The drawings corresponding to the evolution of L_1-norm are placed on the next row. The third row consists of the Fourier transforms of the patterns. The last row shows the wave-number content of the pattern.

In the first numerical experiment (the left column of panels in Fig. 4) we set β to a value, slightly bigger than δ, which is supposed to be a case in the interface between the regions of H^+ and S. Indeed, our simulations show that the system eventually evolves to a state of coexistence of both patterns (designated by SH^+). Note that the system shows a tendency to develop squares close to the sidewalls. There are lines along which the distance between hexagons, and in some cases between squares, is larger than the average one. These lines are "fault lines" across which the neighbouring domains with different patterns slide during the evolution of the pattern towards a steady state. The orientations of the hexagonal and the square lattices are rather deformed and in some regions the directions of the dominant lattice keep rotating in time.

The Fourier transform indicates that the dominant modes fall in a circular ring of nearly critical modes. The modes are somewhat more evenly distributed along the ring than in the cases where the orientation of the lattice is less deformed. The fundamental wave-number here is $q_f = 1.01 q_c$. However, the curve of the wave content as a function of q/q_c (bottom-left panel of Fig. 4) does not suggest the existence of secondary modes, as it is the case in the above treated sets of parameters.

For the second example of coexistence we set β and δ so as to place the system in the limit between the regions of H^- and S. Our results show that it evolves to a coexistence of hexagons and squares, whose pattern is much more ordered than in the previous case. Hexagons appear close to the upper, left and right sidewalls, and also in the lower part of the box when the domain is larger. The squares occupy

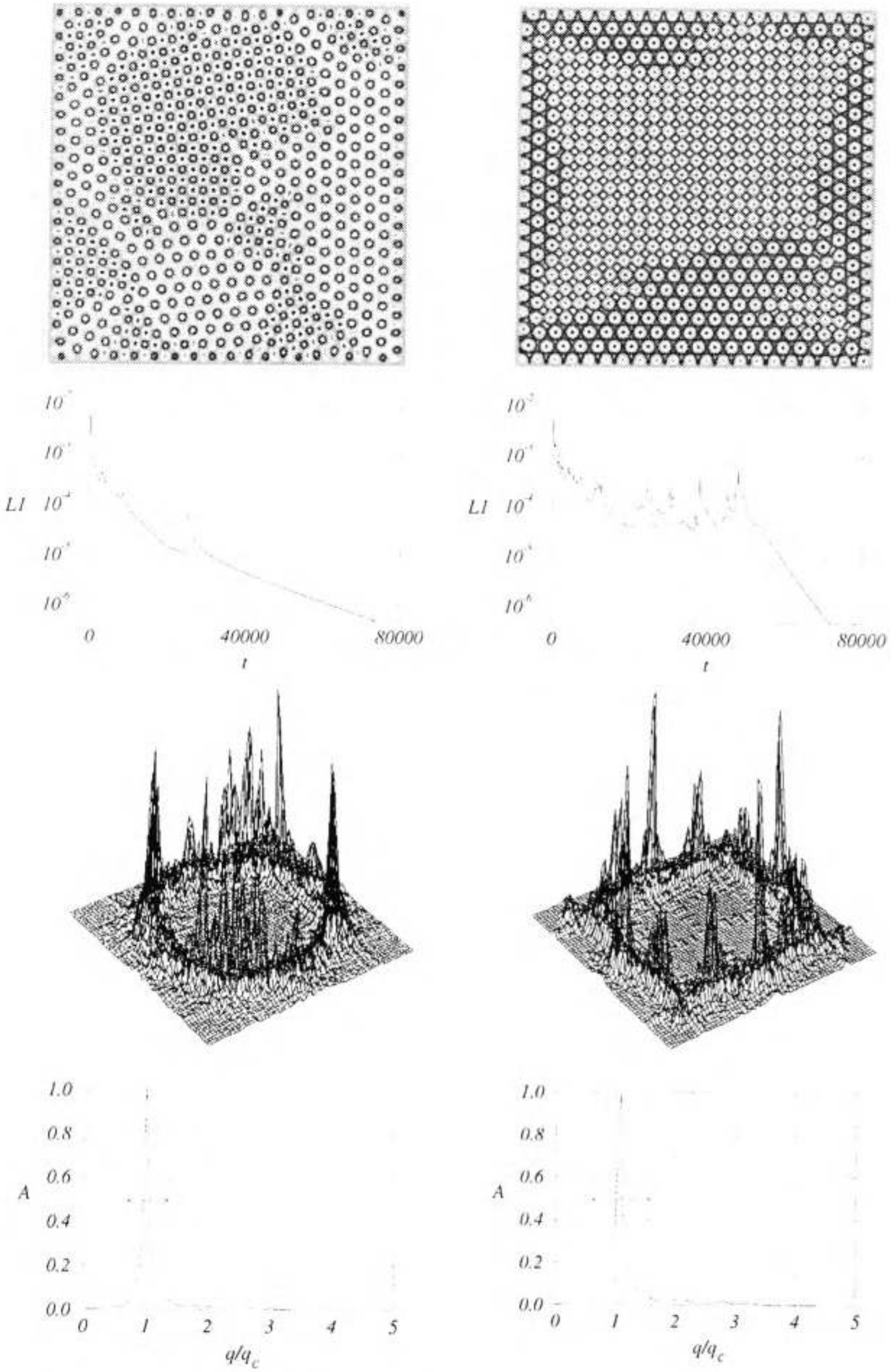

Fig. 4. Coexistence of squares S and hexagons H^+ or H^-. Left panels: SH^+ at $t = 73860$ for $\mu = 2.3$, $\alpha = -0.9$ and $\beta = -0.05\sqrt{7}$, $\delta = -0.07\sqrt{7}$. Right panels: SH^- at $t = 71950$ for $\mu = 2.8$, $\alpha = -0.9$ and $\beta = 0.1\sqrt{7}$, $\delta = 0.17\sqrt{7}$. From top to bottom: the pattern; the time evolution of the L_1-norm; Fourier transform; wave-number content of the pattern shown

mostly the inner part of the system.

The Fourier transform displays a squared structure, which is in a sharp contrast with the circular structure found in the previous case. Each corner of the square contains a small peak. In addition, there are three other peaks along each side of the square totaling twelve along the all four sides. The peak in the center of each side is slightly off the square and the twelve peaks actually fall in a circular ring of fundamental modes. These peaks define two hexagonal lattices rotated by an angle of $\pi/6$ with respect to each other. The hexagons, belonging to one of the lattices, appear close to the left and the right sidewalls of the system. The hexagons, *belonging to the second lattice, appear closer to the upper sidewall.* The two lattices do *not* coexist in the same parts of the configurational space. Both the image of the structure and the associated Fourier transform suggest that the amplitudes of the hexagons, belonging to each lattice, are of the same order, because they belong to the ring of fundamental modes.

The structure of squares results from the superposition of a lattice of fundamental modes with $q = q_f$ and a second one, rotated by an angle of $\pi/4$ relatively to the former and having $q = \sqrt{2}\, q_f$.

A different situation occurs with the other two lattices which are associated with the structure of squares. The first lattice is defined by two directions parallel to the sidewalls and by modes falling in the ring of fundamental modes. The four corresponding peaks in the Fourier transform coincide with those of the two hexagonal lattices which, consequently, are the highest peaks. The second lattice is rotated by an angle of $\pi/4$ with respect to the former, with modes $\sqrt{2}\, q_f$, generated by the nonlinear interaction of the fundamental modes. Here, the two square lattices do coexist in the same physical space.

In the last case the wave-number content of the pattern exhibits a maximum at $q_f = 1.07\, q_c$. The average wave-number, measured according to Eq. (7), is also larger than the critical one.

4.4. PATTERNS FOR VANISHING LINEAR ATTENUATION COEFFICIENT $\alpha = 0$

In this section we discuss the numerical findings for $\alpha = 0$ when, according to dispersion equation, the lower limit of the unstable wave-number is zero. The coefficients of the quadratic terms were selected to place the system in the H^--régime. Then all scales with $q < \sqrt{\mu}$ are supposed to be linearly unstable while the scales with $q > \sqrt{\mu}$ are damped.

The numerically obtained time evolution of the pattern is shown in Fig. 5. Smaller cells are indeed damped first. The more important finding, however, is that the cells increase with time and the system evolves towards a state where a single cell eventually occupies the whole box. This is somewhat counter-intuitive because one might expect in this case an onset of regular pattern with the most unstable wave-number $q_m = \sqrt{\mu/2} = 1$ for the selected value $\mu = 2$. Moreover, the box we have chosen is large enough to harbour more than 12 wave-lengths q_m, and hence this is not an effect connected with the distortion of the fastest-growing modes, due to the lack of space for their spatial extent.

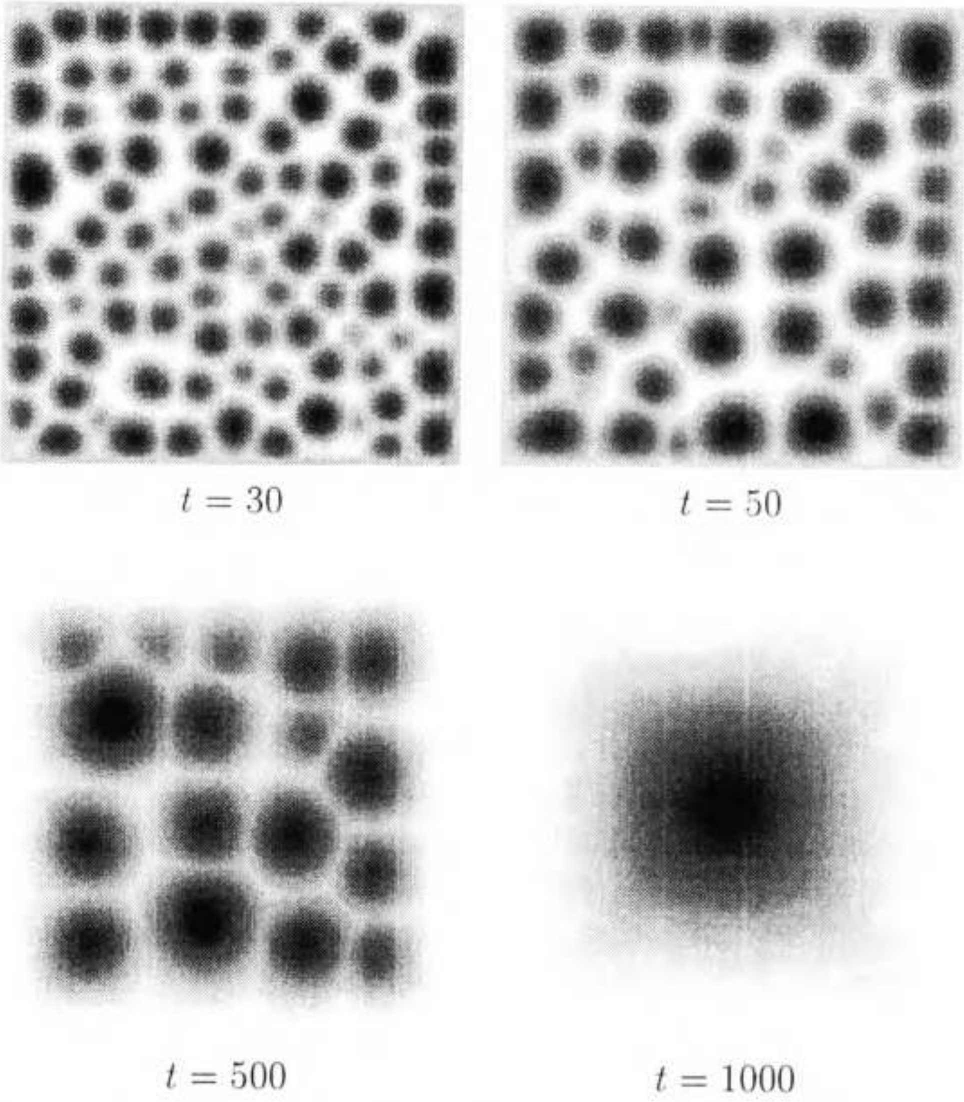
$t = 30$ $t = 50$

$t = 500$ $t = 1000$

Fig. 5. Evolution of the H^--pattern for $\alpha = 0$, $\mu = 2.0$, $\beta = -0.125\sqrt{7}$, and $\delta = 0.75\sqrt{7}$

Thus the interpretation of this simulation is that patterns with a characteristic size of the cell are obtained when larger than the box size wave-lengths are present among the linearly unstable wave-lengths of the system. The evolution eventually ends up in a stationary single-cell state, filling the whole bounding box. The influence of the boundaries on the motion makes the fastest growing (more unstable) modes to disappear eventually and only the largest convective cell, compatible with the box size, survives.

5. CONCLUSIONS

In the present work we investigate the properties of long wave-length patterns formed in systems which evolve according to the non-variational dynamics described by Eq. (1). The non-Boussinesq effects are neglected by setting $\gamma = 0$ in Eq. (1).

We found hexagonal tessellations H^+ (H^-) for $\beta > \delta$ ($\beta < \delta$) and tessellations of squares for $\beta = \delta$. By setting β to a value slightly larger than δ we identified states of coexistence between H^+ and S. Similarly, we found coexisting H^- and S patterns when choosing β to be slightly smaller than δ. These states of coexistence are less robust than those of single patterns. They depend on the forcing applied and on the horizontal dimensions of the system. A change in one of these parameters may lead to the disappearance of one of the patterns.

Typically, the speed of evolution of the patterns shows a rapid decay in the early stages. In the intermediate stages the speed is rather irregular because of the creation or annihilation of cells, transport of dislocations, deformation of grains. These are evolutions of the *phase* of the pattern in general. The last stage is a sustained monotone decay of the L_1-norm, suggesting that the system eventually attains a stationary state. The onset of the sustained decay serves as a criterion to terminate the computations.

The analysis of the spectral content of these patterns reveals that the fundamental wave-number of the structure is very close to the critical. The largest discrepancy occurs in the case of coexistence of hexagons H^- and squares S, where we find a fundamental mode which is 7% larger than the critical. The Fourier analysis also shows the existence of active modes *outside* the band of linearly unstable modes. In the case of single-pattern tessellations, these modes are not merely higher harmonics of the fundamental mode, but they can also originate from the interactions between modes with different orientations and/or wave-numbers. The ability of the system to generate and sustain secondary active modes leads in the case of square patterns to the coexistence, in the same subdomain in the configurational space, of a dominant lattice and a secondary one, the latter slanted by an angle $\pi/4$ with respect to the former.

For $\alpha = 0$ our calculations indicate that all scales shorter than the measures of the box are eliminated as the system evolves in time from a random initial condition. A single-cell stationary pattern is eventually reached, having the largest finite wave-length which is compatible with the dimensions of the box.

For $\kappa = +1$ we observe onset of patterns with larger density of defects when increasing the forcing, but no indication of the existence of possible unsteady asymptotic states. Our preliminary results for the regime $\kappa = -1$ (not shown in the present paper) suggest that at least in two cases there appear unsteady patterns of irregular polygons at high forcing. The numerical interrogation of this case will be published elsewhere.

Acknowledgements. The authors acknowledge fruitful discussions with G. Huang, H. Linde and A. A. Nepomnyashchy.

This work was supported by DGICYT 0.(Spain) under Grant PB 93–81, by the European Union under Grant Network ERBCHRXCT 93–107 and by "Fundación Ramón Areces". J.P. also acknowledges the support of a post-doctoral fellowship from the Spanish Ministry of Education and Science and fellowship No. 30167895-2 from the Brazilian National Council for the Research and Development (CNPQ).

The work of C.I.C. is supported in part by Grant LEQSF(1999-2002)-RD-A-49 from the Louisiana Board of Regents.

REFERENCES

1. Bestehorn, M. Phase instabilities for Bénard-Marangoni convection in fluid layers with large aspect ratio. *Phys. Rev. E*, **48**, 1993, 3622–3634.
2. Bestehorn, M. Square patterns in Bénard-Marangoni convection. *Phys. Rev. Lett.*, **76**, 1996, 46–49.
3. Block, M. J. Surface tension as the cause of Bénard cells and surface deformation in a liquid film. *Nature*, **178**, 1956, 650–651.
4. Chapman, C. J., M. R. E. Proctor. Non-linear Rayleigh-Bénard convection between poorly conducting boundaries. *J. Fluid Mech.*, **101**, 1980, 759–782.
5. Christov, C. I., J. Pontes, D. Walgraef, M. G. Velarde. Implicit time splitting for fourth-order parabolic equations. *Comp. Meth. Appl. Mech. & Eng.*, **148**, 1997, 209–224.
6. Cross, M. C., P. C. Hohenberg. Pattern formation outside of equilibrium. *Rev. Mod. Phys.*, **65**, 1993, 851–1112.
7. Douglass, J., H. H. Rachford. On the numerical solution of heat conduction problems in two and three space variables. *Trans. Amer. Math. Soc.*, **82**, 1956, 421–439.
8. Knobloch, E. Pattern selection in long wavelength convection. *Physica D*, **41**, 1990, 450–479.
9. Knobloch, E. Onset of zero Prandtl number convection. *J. Phys. II France*, **2**, 1992, 995–999.
10. Koschmieder, E. L. Bénard cells and Taylor vortices. Cambridge Univ. Press, Cambridge, UK, 1993.
11. Kubstrup, C., H. Herrero, C. Pérez-Garcia. Fronts between hexagons and squares in a generalized Swift-Hohenberg equation. *Phys. Rev. E*, **54**, 1996, 1560–1569.
12. Normand, C., Y. Pomeau, M. G. Velarde. Convective instability: A physicist's approach. *Rev. Mod. Phys.*, **49**, 1977, 581–624.
13. Pearson, J. R. A. On convection cells induced by surface tension. *J. Fluid Mech.*, **4**, 1958, 89–500.
14. Shtilman, L., G. Sivashinsky. Hexagonal structure of large-scale Marangoni convection. *Physica D*, **52**, 1991, 477–488.
15. Sivashinsky, G. I. Large cells in nonlinear Marangoni convection. *Physica D*, **4**, 1982, 227–235.
16. Sivashinsky, G. I. On cellular instability in the solidification of a dilute binary alloy. *Physica D*, **8**, 1983, 243–248.
17. Skeldon, A. C., M. Silber. New stability results for patterns in a model of long wavelength convection. *Physica D*, **122**, 1998, 117–133.
18. Thess, A., M. Bestehorn. Planform selection in Bénard-Marangoni convection: *l* hexagons versus *g* hexagons. *Phys. Rev. E*, **52**, 1995, 6358–6367.
19. Tribelsky, M. I., S. Kai, H. Yamazaki, M. G. Velarde. Universal spatiotemporal scaling

in the dynamics of one-dimensional pattern selection. *Phys. Rev. E*, **51**, 1995, 5132–5135.

20. Velarde, M. G., C. Normand. Convection. *Sci. Am.*, **243**, 1980, 92–108.
21. Yanenko, N. N. Method of fractional steps. Gordon and Breach, NY, 1971.

Received March 24, 2000

J. PONTES
Dept. of Metallurgical
and Material Engineering
COPPE/UFRJ, PO Box 68505
21945-970 Rio de Janeiro, RJ
BRAZIL

C. I. CHRISTOV
Corresponding author
Department of Mathematics
University of Louisiana, Lafayette
LA 70504-1010, USA
E-mail: `christov@louisiana.edu`

M. G. VELARDE
Instituto Pluridisciplinar
Universidad Complutense de Madrid
Paseo Juan XXIII No. 1
E-28040 Madrid, SPAIN